Comparison of Americium-241 and Technetium-99m as Transmission Sources for Attenuation Correction of Thallium-201 SPECT Imaging of the Heart

Edward P. Ficaro, Jeffrey A. Fessler, W. Leslie Rogers and Markus Schwaiger

Department of Internal Medicine, Division of Nuclear Medicine, The University of Michigan Medical Center, Ann Arbor, Michigan

This study compares the ability of ^{241}Am and ^{99m}Tc to estimate ^{201}Tl attenuation maps while minimizing the loss in the precision of the emission data. **Methods:** A triple-head SPECT system with either an ^{241}Am or ^{99m}Tc line source opposite a fan-beam collimator was used to estimate attenuation maps of the thorax of an anthropomorphic phantom. Linear attenuation values at 75 keV for ^{201}Tl were obtained by linear extrapolation of the measured values from ^{241}Am and ^{99m}Tc. **Results:** Lung and soft-tissue estimates from both isotopes showed excellent agreement to within 3% of the measured values for ^{201}Tl. Linear extrapolation did not yield satisfactory estimates for bone from either ^{241}Am (+11.7%) or ^{99m}Tc (−15.3%). Patient data were used to estimate the dependence of crosstalk on patient size. Contamination from ^{201}Tl in the transmission window was 5–6 times greater for ^{241}Am compared to ^{99m}Tc, while the contamination in the ^{201}Tl data in the transmission-emission detector head (head 1) was 4–5 times greater for ^{99m}Tc compared to ^{241}Am. No contamination was detected in the ^{201}Tl emission data of heads 2 and 3 from ^{241}Am, whereas the ^{99m}Tc produced a small crosstalk component giving a signal-to-crosstalk ratio near 20:1. Measurements with a fillable chest phantom estimated the mean error introduced into the data from the removal of the crosstalk. **Conclusion:** Based on the measured data, ^{241}Am is a suitable transmission source for simultaneous transmission-emission tomography for ^{201}Tl cardiac studies.

Key Words: transmission tomography; SPECT; attenuation correction; cardiac imaging

J Nucl Med 1994; 35:652–663

In SPECT, photon attenuation in the body is a significant process which strongly affects quantitative precision in determining in vivo radiopharmaceutical tissue concentrations. This phenomenon is particularly pronounced in cardiac SPECT imaging using ^{201}Tl due to the inhomogeneous composition of the thorax and the low photon energy of ^{201}Tl. As a result, attenuation correction techniques that assume uniform attenuation within the body produce image artifacts and inaccurate estimates for cardiac radiotracer uptake. The most promising method for correcting SPECT images for photon attenuation is to measure attenuation distribution using transmission computed tomography (TCT) and iteratively reconstruct the emission images using the measured nonuniform attenuation maps (*1–10*).

Because the acquisition of individual transmission and emission scans undesirably increases patient imaging time, commercially available SPECT systems have been modified to acquire transmission and emission projections simultaneously (*7–9*). An important decision in the development of these systems is the choice of isotope for the transmission source. This source should perform the following functions: (1) minimize crosstalk between the transmission and emission energy windows, (2) provide accurate attenuation maps for radiotracer energy and (3) be simple to use in a clinical environment. Energy window crosstalk results in the recording of photon counts that do not carry information on the measured process. More explicitly, if a transmission photon, directly or indirectly, produces a count in the emission window, crosstalk has occurred from the transmission to the emission window. It is important to minimize crosstalk to ensure the precision of the measured data.

The objective of this work was to evaluate possible transmission sources based on half-life, photon emission spectrum, transmission properties, and the energy window crosstalk for correcting ^{201}Tl cardiac studies. A list of available isotopes for performing transmission imaging is presented in Table 1. The criteria were: (1) primary photon emissions between 40 keV and 160 keV so that low-energy collimators can be used, (2) the absolute yield for photon emission should be greater than 2% to minimize source size and (3) a half-life greater than 180 days to eliminate periodic refilling or replacement of the source. Included at the bottom of this table are the low-energy isotopes used rou-

Received Jun. 22, 1993; revision accepted Dec. 29, 1993.
For correspondence or reprints contact: Edward Ficaro, PhD, The University of Michigan Hospitals, 1500 E. Medical Center Dr., Ann Arbor, MI 48109.

TABLE 1
Available Isotopes for Performing Low-Energy Transmission Tomography*

Isotope	Decay mode	Photon emissions energy (keV) and (yield)	K shell x-ray emissions energy (keV) and (yield)	Half-life
^{241}Am	α	59.4 (35.9%)	—	432.2 yr
^{109}Cd	EC	88.0 (3.61%)	22.0–25.5 (99.5%)	462.9 days
^{153}Gd	EC	97.4 (27.6%), 103.2 (19.6%)	40.9–48.3 (118.6%)	241.6 days
^{195}Au	EC	98.9 (10.9%), 129.8 (0.82%)	65.1–77.9 (97.9%)	183.0 days
^{57}Co	EC	122.1 (85.9%), 136.5 (10.3%)	—	271.8 days
^{201}Tl	EC	135.3 (2.65%), 167.4 (10.0%)	68.9–82.6 (93.8%)	73.1 hr
^{99m}Tc	IT	140.5 (89.1%)	18.2–20.6 (5.77%)	6.01 hr
^{123}I	EC	159.0 (83.3%)	27.2–31.7 (86.4%)	13.2 hr

*Decay scheme data taken from References 11 and 12.
EC = electron capture and IT = isomeric transition.

tinely in nuclear medicine, ^{201}Tl, ^{99m}Tc and ^{123}I. From the list of sources, ^{241}Am was the most appealing because of its long half-life and its photon energy is below the photopeaks of ^{201}Tl. However, ^{99m}Tc has been the most popular isotope for transmission measurements due to its clinical availability. It was our hypothesis that the properties of ^{241}Am are more suitable than those of ^{99m}Tc for transmission imaging during ^{201}Tl cardiac studies. To test this assumption, phantom studies were used to determine the quality of the measured attenuation maps and the precision with which these maps could be extrapolated to the energy of ^{201}Tl. In addition, patient studies and a second set of phantom measurements were employed to measure the crosstalk between the transmission and emission windows and the amount of noise introduced into the measurement as a result of crosstalk corrections.

THEORY

Energy Window Crosstalk and Compensation Techniques

The decay of ^{201}Tl produces gamma rays with energies of 135 and 167 keV and mercury x-rays with energies varying between 68.9 and 82.6 keV. For a ^{201}Tl cardiac study, projection data are typically collected in windows centered at 74 keV for the mercury x-rays and at 167 keV to detect the high energy gamma rays of ^{201}Tl. The decay of ^{241}Am produces a gamma ray with an energy of 60 keV. Due to the energy resolution of NaI(Tl) scintillators, the ^{241}Am and the mercury x-ray photopeaks overlap, introducing a bidirectional source of crosstalk contamination between transmission and emission data. Contamination in the ^{241}Am window from the high energy gammas of ^{201}Tl is insignificant compared to the photopeak overlap. For ^{99m}Tc, the contamination of the ^{201}Tl data results from: (1) the emission of lead x-rays due to photon interactions in the collimator and shielding of the detector, (2) overlap between the 167-keV photopeak of ^{201}Tl and the 140-keV peak of ^{99m}Tc, and (3) multiply scattered 140-keV photons. The contamination of ^{99m}Tc data from ^{201}Tl photons results from the overlap between the 140-keV photopeak of ^{99m}Tc and the 135-keV and 167-keV photopeaks of ^{201}Tl. Photons emitted at 167 keV experiencing small angle scatters will also contaminate the 140-keV ^{99m}Tc energy window.

As a result of the crosstalk described above, the true, uncontaminated emission (P_e) and transmission (P_t) rates are determined from the measured emission (M_e) and transmission (M_t) rates using

$$P_e(x, y, \theta) = M_e(x, y, \theta) - b_e(x, y, \theta) \quad \text{Eq. 1A}$$

$$P_t(x, y, \theta) = M_t(x, y, \theta) - b_t(x, y, \theta), \quad \text{Eq. 1B}$$

where (x, y) is the projection pixel location, θ is the projection angle, and b_e and b_t are the crosstalk contributions in the emission and transmission windows, respectively. In choosing the isotope for the transmission source, one attempts to maximize the signal-to-crosstalk ratio

$$S_i(x, y, \theta) = \frac{P_i(x, y, \theta)}{b_i(x, y, \theta)}, \quad \text{Eq. 2}$$

where the subscript i = e, t represents the emission and transmission measurements, respectively. More importantly, methods must be developed to measure or estimate crosstalk, $b_e(x, y, \theta)$ and $b_t(x, y, \theta)$, so that the introduction of error into $P_e(x, y, \theta)$ and $P_e(x, y, \theta)$ is minimized.

For a single detector SPECT system, $b_e(x, y, \theta)$ and $b_t(x, y, \theta)$ cannot be directly measured unless separate transmission and emission acquisitions are performed at the cost of increased imaging time. As a result, one assumes that the contamination terms $b_e(x, y, \theta)$ and $b_t(x, y, \theta)$ are proportional to $P_t(x, y, \theta)$ and $P_e(x, y, \theta)$, respectively, so that Equations 1A and B can be rewritten (*8*) as

$$P_e(x, y, \theta) = M_e(x, y, \theta) - f_e(x, y, \theta)P_t(x, y, \theta) \quad \text{Eq. 3A}$$

$$P_t(x, y, \theta) = M_t(x, y, \theta) - f_t(x, y, \theta)P_e(x, y, \theta), \quad \text{Eq. 3B}$$

where $f_e(x, y, \theta) = b_e(x, y, \theta)/P_t(x, y, \theta)$ and $f_t(x, y, \theta) = b_t(x, y, \theta)/P_e(x, y, \theta)$. Using Equations 3A and B, the true, uncontaminated rates can be calculated from

$$P_e(x, y, \theta) = \frac{M_e(x, y, \theta) - f_e(x, y, \theta)M_t(x, y, \theta)}{1 - f_e(x, y, \theta)\, f_t(x, y, \theta)} \quad \text{Eq. 4A}$$

and

$$P_t(x, y, \theta) = \frac{M_t(x, y, \theta) - f_t(x, y, \theta)M_e(x, y, \theta)}{1 - f_e(x, y, \theta)\, f_t(x, y, \theta)}. \quad \text{Eq. 4B}$$

Using a ^{99m}Tc transmission source, Frey et al. demonstrated that $f_e(x, y, \theta)$ and $f_t(x, y, \theta)$ can be estimated empirically from additional measurements (*8*) with a marginal increase in bias to the estimation of $P_e(x, y, \theta)$ and $P_t(x, y, \theta)$. For the purpose of this work, $f_e(x, y, \theta)$ and $f_t(x, y, \theta)$ will be used to quantify the relative contamination rates between the transmission windows of ^{241}Am and ^{99m}Tc with the emission windows of ^{201}Tl.

A triple-head system (cf. Fig. 1) has the advantage of measuring $b_{t1}(x, y, \theta)$ (numeric subscript denotes head number) directly, since $P_{t2}(x, y, \theta) = P_{t3}(x, y, \theta) = 0$. Provided the camera heads collect data in the transmission window over 360°, $b_{t1}(x, y, \theta)$ can be estimated by

$$b_{t1}(x, y, \theta) = \frac{\varepsilon_1}{\varepsilon_2} T(x' \rightarrow x, y' \rightarrow y, \theta' \rightarrow \theta) b_{t2}(x', y', \theta'), \quad \text{Eq. 5}$$

where

$\varepsilon_1, \varepsilon_2$ = the extrinsic sensitivities of heads 1 and 2, respectively,

$b_{t2}(x, y, \theta)$ = the measured contamination in the transmission window of head 2,

$T(x' \rightarrow x, y' \rightarrow y, \theta' \rightarrow \theta)$ = transformation matrix converting the collimator geometry of head 2 to the collimator geometry of head 1. The matrix is unity for identical collimators.

For detector heads with identical collimators and crystals, Equation 5 reduces to $b_{t1}(x, y, \theta) = b_{t2}(x, y, \theta)$, and $P_t(x, y, \theta)$ is determined from $M_t(x, y, \theta)$ by simple subtraction.

In correcting the emission data from the detector collecting both transmission and emission data (head 1 of Fig. 1), we approximate the contamination term $b_e(x, y, \theta)$ by

$$b_e(x, y, \theta) = c_e(t)P_{t0}(x, y), \quad \text{Eq. 6}$$

where

$c_e(t)$ = the fraction of the transmission photon flux detected in the ^{201}Tl window as a function of tissue thickness, t,

$t(x, y, \theta)$ = the measured equivalent tissue thickness, $\frac{1}{\mu_t^{tis}} \ln\left(\frac{P_{t0}(x,y)}{P_t(x,y,\theta)}\right)$

μ_t^{tis} = the linear attenuation coefficient for tissue,

$P_{t0}(x, y)$ = transmission photon flux without an absorber present, commonly referred to as a "blank" scan.

Typically, $c_e(t)$ is an empirical correction based on independent measurements using known equivalent thicknesses of tissue.

For the emission data from detector heads 2 and 3, no correction is necessary for an ^{241}Am transmission source, since $b_{e2}(x, y, \theta) = b_{e3}(x, y, \theta) = 0$. For a ^{99m}Tc transmission source, Tung et al. (*9*) developed an approximate method for estimating $b_e(x, y, \theta)$ for heads 2 and 3. Provided heads 2 and 3 are fitted with similar collimators and collect data in the emission window over 360°, $b_{e2}(x, y, \theta)$ is estimated using

$$b_{e2}(x, y, \theta) = \text{MAX}\,[0, M_{e2}(x, y, \theta) - M_{e3}(x, y, \theta)]. \quad \text{Eq. 7}$$

Because $b_{e2}(x, y, \theta)$ is not measured independently, this correction process biases the estimate of $P_{e2}(x, y, \theta)$. Equations 6 and 7 extend logically to head 3.

Calculating Linear Attenuation Coefficients

In narrow-beam geometry, the transmission of monoenergetic photons through an absorber of thickness t follows the exponential relationship

$$I(t) = I_0 e^{-\int_0^t \mu_t(l)\, dl}, \quad \text{Eq. 8}$$

where I(t) and I_0 are the measured photon intensities with and without the absorber present, and $\mu_t(l)$ is the total linear attenuation coefficient in dl at l. If the absorber is homogeneous, the linear attenuation coefficient is determined from

$$\mu_t = \frac{1}{t} \ln\left(\frac{I_0}{I(t)}\right) \quad \text{Eq. 9}$$

In a TCT measurement, transmitted photon intensities are measured in two dimensions (x, y) at multiple angles θ. I_0 is a "blank" scan acquired in the same geometry at a single angle without the absorber present. Using this data, the natural logarithm of the measured ratio, $C(x, y, \theta)$, of blank-to-transmitted counts is computed

$$C(x, y, \theta) = \ln\left(\frac{I_0(x, y)}{I(x, y, \theta)}\right) = \int_0^t \mu_t(l)\, dl, \quad \text{Eq. 10}$$

which is input to the reconstruction process to determine $\mu_t(l)$.

Converting Measured Attenuation Map to Emission Energy

Since photon attenuation is dependent on photon energy, the measured μ_t values from the reconstructed transmission sinograms must be converted to the energy of the emission photons. A commonly used method assumes that μ_t varies linearly between the emission (E_e) and transmission (E_t) energies, and thus, the measured transmission

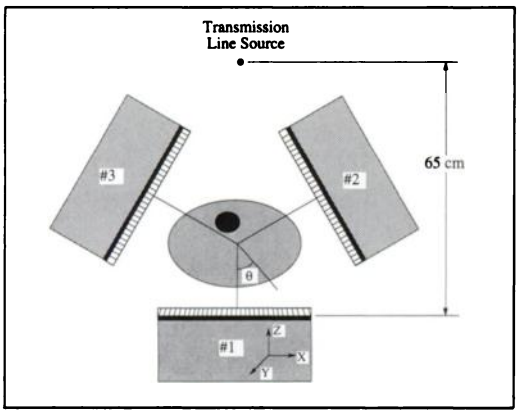

FIGURE 1. Geometry for a simultaneous transmission-emission tomography system using a triple-head camera.

coefficient values $\mu_t(E_t)$ can be extrapolated to the emission energy $\mu_t(E_e)$ using the following equation

$$\mu_t(E_e) = \frac{\mu_t^{tis}(E_e)}{\mu_t^{tis}(E_t)}\,\mu_t(E_t), \qquad \text{Eq. 11}$$

where $\mu_t^{tis}(E_e)$ and $\mu_t^{tis}(E_t)$ are the linear attenuation coefficients of tissue for the emission and transmission isotopes, respectively. In this work, we have used μ_t^{tis} (75 keV) = 0.183/cm for ^{201}Tl emission photons and μ_t^{tis} (60 keV) = 0.197/cm and μ_t^{tis} (140 keV) = 0.153/cm for ^{241}Am and ^{99m}Tc transmission photons, respectively (values from Reference 13).

For photons with energies between 60 and 165 keV, the primary interactions represented by μ_t are photoelectric absorption and Compton scattering. In the thorax, lungs, heart and body wall are comprised of low Z elements for which Compton scattering is the predominant interaction. For these compositions, Equation 11 is applicable, since the Compton interaction is a slowly decreasing function of energy. However, for high Z elements such as calcium in bone, the photoelectric probability, which increases proportionally with Z^4, becomes more prevalent, and it has an energy dependence of E^{-3}. Therefore, for emission and transmission photons of different energy, Equation 11 is expected to be a poor approximation for bone.

METHODS

Imaging System

Transmission imaging was performed using the PRISM 3000 SPECT system (Ohio Imaging of Picker International, Bedford Heights, OH) with a collimated line source holder attached to the rotating gantry opposite and parallel to a camera head fitted with a low-energy, general-purpose, fan-beam collimator with a focal length of 65 cm as shown in Figure 1. Low-energy, high-resolution, parallel-hole collimators were fitted to heads 2 and 3. Since the holder cannot currently move radially, only circular orbits are permitted so that the source remains at the focal distance of the collimator. The source is positioned after the radius of rotation has been determined from the patient outline. The holder accommodates a 3.0-mm o.d. × 240 mm (active length) line source and provides variable collimation in both the radial and axial directions. For this work, the line source was radially collimated to a 50° fanbeam, and axial collimation was achieved with 50.8 × 25.4 × 0.25-mm strips of lead foil separated by 1.59-mm thick foam spacers. The transmission sources consisted of a 5.55 GBq (150 mCi) ^{241}Am line source (Isotope Products Laboratories, Burbank, CA) sealed in a 0.30-mm thick stainless steel tube (3 mm o.d. × 240 mm) and a 0.444-GBq (12 mCi) ^{99m}Tc line source contained in a 0.9-mm thick glass tube (3 mm o.d. × 240 mm). The activity of the ^{99m}Tc source was chosen to provide transmission rates comparable to the ^{241}Am source in the posterior of view in patients.

For the phantom and patient SPECT studies, projection data were acquired in a 64 × 64 matrix by all heads every 6° over 360° at 16 sec per step for a total scan time of 20 min. Transmission energy windows of 59.0 ± 5.9 keV and 140.0 ± 10.5 keV were used for ^{241}Am and ^{99m}Tc, respectively. Two energy windows, one at 74.0 ± 9.25 keV and the other at 167 ± 12.5 keV, were summed to record ^{201}Tl emission data. For each study, projection data from the three detector heads were acquired simultaneously in both the transmission and the summed ^{201}Tl windows.

Attenuation Map Measurements

The attenuation map measurements were performed using an anthropomorphic phantom (Fission Product Phantom, Humanoid Systems, Carson, CA) with stub arms and legs. This phantom provides a realistic representation of the human body from the head to the pubis. The fillable organs (stomach, liver, kidneys, pancreas and spleen) contained water. All other structures and organs, including the heart and lungs, are solid materials fashioned for tissue radioequivalent attenuation. Transmission data were recorded with and without the axial source collimator to determine the effect of source collimation on μ_t and the crosstalk from the transmission to emission window.

For the ^{241}Am transmission source, the recorded count rates in the ^{241}Am window for the collimated line source were 15.2 kcps and 7.7 kcps for the posterior and left lateral views, respectively. Transmission photons detected outside of the body outline were not included in these count rates. Recorded count rates with the source uncollimated were approximately 1.7 times greater. For the blank scans, a 0.762-mm thick, curved film of lead was placed along the length of the source to reduce incident photon flux and minimize deadtime losses. With this attenuator in place, 30 million (30M) count blank scans were acquired in 27.2 and 15.8 min for the collimated and uncollimated source, respectively.

For the ^{99m}Tc transmission source, the recorded count rates in the ^{99m}Tc window for the collimated line source were 15.8 kcps and 8.8 kcps for the posterior and left lateral views, respectively. Count rates without the axial source collimator were approximately 1.6 times greater than with source collimation. For the blank scans, 1.02 mm of lead was used to attenuate photon flux to reduce deadtime losses. With this setup, 30M count blank scans were acquired in 20.0 and 12.6 min for the collimated and uncollimated source, respectively. The blank scan data was decay-corrected to the start of the TCT scan.

Transmission projection images were also acquired with a collimated, 11.8 MBq (320 μCi) ^{201}Tl source in a 0.9-mm thick glass tube (3 mm o.d. × 240 mm). Because the count rate for this source was so low, projection data were acquired for 15 min at each angle to achieve comparable counting statistics to the ^{241}Am and ^{99m}Tc scans. At the completion of the TCT scan, a 30M blank image was acquired in 1.2 hr. With the source removed, a 15-min background image was acquired to correct the projection data for natural background contamination. The blank scan and the projection

images at each angle were decay-corrected to the start of the TCT scan.

To determine reference μ_t values for the different structures in the phantom thorax, the individual organs (bone, heart, lung and liver) were removed and narrow-beam transmission measurements were performed using small hole apertures, 6.35 mm o.d. × 25.4 mm in length, on a HPGe detector and 2.54-cm disk sources of ^{241}Am, ^{99m}Tc and ^{201}Tl. The source-to-detector distance was fixed at 15 cm, and the attenuation of air was ignored. Transmission photopeak count rates were recorded with known thicknesses (error ±3%) of the materials in and out of the collimated transmission photon beam.

Crosstalk Measurements

Patient Studies. For the patient studies, crosstalk contamination was measured as a function of patient size. The patients were a 1.73-m tall, 57-kg female (Patient 1), a 1.70-m tall, 75-kg male (Patient 2) and a 1.80-m tall, 95-kg male (Patient 3). Patients were imaged supine with their arms above their heads, and the camera orbit radius was determined by placing the camera head to within 1–2 cm of the patient's body in the lateral position. Thallium-201 count rates measured in the right anterior oblique (RAO) position by head 2 were 2.3 kcps, 2.0 kcps and 1.0 kcps for the small (Patient 1), medium (Patient 2) and large (Patient 3) patients, respectively. To measure the contamination of the emission data from transmission photons, transmission projection data using a 5.55-GBq (150 mCi) ^{241}Am and a 444-MBq (12 mCi) ^{99m}Tc source was acquired prior to the injection of ^{201}Tl. The contamination of the transmission data from emission photons was measured following the injection of 111 MBq (3 mCi) of ^{201}Tl with the transmission source removed.

Phantom Study. To estimate the error introduced into the reconstructed, attenuation-corrected emission images due to the presence and removal of crosstalk in the emission and transmission data, an elliptical cylinder with lung, spine and cardiac inserts (Data Spectrum Corp., Chapel Hill, NC) was imaged. To simulate 6% uptake in the myocardium following an injection of 111 MBq (3 mCi) ^{201}Tl, the heart chamber was filled with 56 kBq/ml and the body and lungs were filled with 11 kBq/ml ^{201}Tl. A series of four acquisitions were performed, each acquiring sixty 16-sec projections in the transmission and emission windows over 360°. The acquisitions were as follows:

1. Americium-241 source with no ^{201}Tl in phantom, ((a) Am and (b) Tl windows)
2. Technetium-99m source with no ^{201}Tl in phantom, ((a) Tc and (b) Tl windows)
3. No source with 90 MBq of ^{201}Tl in phantom, ((a) Tc and (b) Tl windows)
4. No source with 90 MBq of ^{201}Tl in phantom, ((a) Am and (b) Tl windows)

The phantom was laser-realigned on the imaging table following injection and mixing of ^{201}Tl in the phantom between acquisition Steps 2 and 3.

To estimate the crosstalk correction factor $c_e(t)$ in Equation 6, the detected counts in each ^{201}Tl photon energy window were recorded as a function of lucite thickness for both ^{241}Am and ^{99m}Tc transmission sources. In these measurements, the line source was located 65 cm from a parallel-hole collimator and plates of lucite (40 × 40 × 1 cm) were placed on top of the collimator to provide overall thicknesses ranging from 1.0 to 23.0 cm. The value for $c_e(t = 0)$ was measured with the source at the focal distance of a 65-cm fan-beam collimator. Each measurement was corrected for natural background radiation, and the tissue equivalent thickness was computed using $t_{tissue} = (\mu_t^{lucite}(E_t)/\mu_t^{tissue}(E_t))t_{lucite}$.

Data Processing

Attenuation Map Measurements. Attenuation line length sinograms were computed from the natural log of the ratio of blank-to-measured transmission counts as outlined by Equation 10. Measured scale corrections were applied to the ^{241}Am and ^{99m}Tc blank scans to account for the lead attenuators used to decrease the photon flux. Transaxial slices through the torso were obtained by iteratively reconstructing (32 iterations) the line length sinograms with a penalized, weighted least-squares (PWLS) algorithm (*14,15*) utilizing an elliptical support to reduce the effects of data truncation. Although, the issue of data truncation from fan-beam geometry is important (*16,17*), it is beyond the scope of this paper; thus, our analysis will be restricted to the nontruncated regions of the reconstructed slices.

From the reconstructed attenuation maps, average μ_t values were calculated from three-dimensional regions drawn within different tissue types present in the phantom. These values were calculated for scans acquired with collimated and uncollimated ^{241}Am and ^{99m}Tc transmission sources and for the collimated ^{201}Tl source. The collimated μ_t values measured by ^{241}Am and ^{99m}Tc were extrapolated to estimate μ_t values for ^{201}Tl at 75 keV using Equation 11. From the narrow-beam measurements for ^{241}Am, ^{99m}Tc and ^{201}Tl, reference μ_t values for the phantom were calculated using Equation 9.

Crosstalk Measurements. For each patient, total projection counts in the transmission and emission windows were used to compute $f_t(\theta)$, $f_e(\theta)$ and $b_{e2}(\theta)$ as a function of projection angle θ. Transmission photons streaming outside of the patient boundary were not used in determining $f_t(\theta)$ and $f_e(\theta)$. The projection angle θ was measured relative to the posterior view in a counter-clockwise direction.

With the elliptical chest phantom data, three datasets were constructed. The reference was an uncontaminated dataset consisting of uncontaminated ^{241}Am and ^{99m}Tc transmission data (acquisitions 1a and 2a) and ^{201}Tl emission data of acquisition 3a. A contaminated data set was constructed by adding projections from acquisitions with identical windows (Am: 1a + 4a, Tc: 2a + 3a, Am contaminated Tl: 1b + 3b, Tc contaminated Tl: 2b + 3b). The contaminated datasets were constructed in this manner as opposed to a simultaneous transmission/emission measurement so that the difference between the contaminated and uncontaminated reconstructed images reflects only the presence of crosstalk and not the variance from separate measurements due to counting statistics. Using the crosstalk removal methods outlined by Equations 5–7, the contaminated data was corrected for crosstalk producing the third dataset. The error in the reconstructed images will be estimated by comparing the corrected and uncontaminated reconstructed images. Because there is no detectable contamination in the ^{201}Tl data of head 2 for an ^{241}Am transmission source, uncontaminated ^{201}Tl data was also used in the contaminated and corrected emission datasets for ^{241}Am.

For each dataset, attenuation maps were reconstructed from transmission data using 32 iterations of the PWLS algorithm with the known boundary support. The attenuation maps were then scaled for 75-keV photons using Equation 11, and emission images were iteratively reconstructed (24 iterations) using the scaled attenuation maps in the forward- and backprojection steps of the

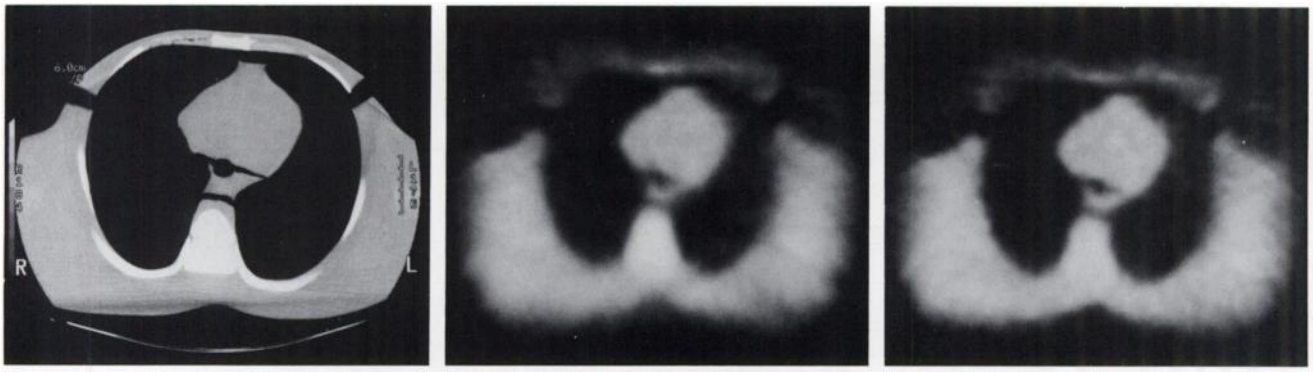

FIGURE 2. Mid-ventricular transmission slice in the thorax of an anthropomorphic phantom using an x-ray scanner (A), a collimated ^{241}Am line source (B) and a collimated ^{99m}Tc line source (C).

PWLS algorithm. Because the attenuated forward- and backprojectors are coded for parallel rays, the emission sinograms of head 1 were rebinned from fan-beam to parallel-hole coordinates prior to reconstruction.

RESULTS

Attenuation Coefficients

Attenuation maps reconstructed from the projection data are displayed in Figure 2. An x-ray CT image of the same slice is included as an anatomical reference. Both ^{241}Am and ^{99m}Tc exhibited good contrast between the heart, lungs, body wall and spine. The spine is more apparent in the ^{241}Am image compared to ^{99m}Tc due to the higher bone tissue contrast inherent at lower photon energies. Line source collimation did not produce visible changes in image contrast or resolution.

Average μ_t values were calculated from three-dimensional regions drawn within different tissue types present in the phantom's thorax. These values are tabulated in Table 2 for scans acquired with collimated and uncollimated ^{241}Am and ^{99m}Tc transmission sources. Measured narrow-beam μ_t values are provided in the table as references. In this table, good agreement was seen between the regional and reference μ_t values. The μ_t values from Table 2 for collimated ^{241}Am and ^{99m}Tc sources were extrapolated to estimate μ_t values for ^{201}Tl at 75 keV using Equation 11. These estimates are presented in Table 3. Linear extrapolation produced suitable estimates for the lung, liver and heart, but appreciable error was obtained for the phantom spine and human bone estimates.

Crosstalk Contamination

From the patient emission data, the measured crosstalk fraction $f_t(\theta)$ is displayed as a function of the projection angle in Figure 3. The crosstalk of ^{201}Tl into the ^{241}Am transmission data is approximately five times greater than the ^{201}Tl scatter into the ^{99m}Tc window. The crosstalk fraction $f_t(\theta)$ is weakly dependent on θ and patient size, where the difference in the mean f_t value between the largest and smallest patient is 5.4% and 7.1% for ^{241}Am and ^{99m}Tc, respectively. The increase in f_t for larger patients results from the increased scattering that shifts more mercury x-rays into the ^{241}Am window and more 167-keV gamma rays from ^{201}Tl into the ^{99m}Tc energy window.

From the patient transmission data, the crosstalk fraction $f_e(\theta)$ for detector head 1 is displayed as a function of θ in Figure 4. Whereas the crosstalk fraction $f_e(\theta)$ for ^{241}Am is nearly constant at 0.026 over all θ for all patients, the ^{99m}Tc crosstalk into the ^{201}Tl window is approximately five times greater in magnitude and is dependent on patient size and projection angle. The behavior of $f_e(\theta)$ is more clearly illustrated by the crosstalk correction factor $c_e(t)$ deter-

TABLE 2
Measured Regional TCT μ_t Values in Anthropomorphic Phantom

	μ_t for ^{241}Am			μ_t for ^{99m}Tc		
Region	Expected*	Collimated†	Uncollimated	Expected	Collimated	Uncollimated
Heart	0.208	0.200	0.197	0.158	0.160	0.158
Liver	0.199	0.203	0.200	0.153	0.152	0.149
Lung	0.0535	0.0535	0.0504	0.0405	0.0412	0.0399
Spine	0.348	0.338	0.332	0.201	0.209	0.205

*Expected values were measured in narrow-beam geometry with a HPGe detector and a point source. The mean percent error is 3%–4%.
†Collimated and uncollimated data represent reconstructed values from transmission transaxial slices with and without axial collimation on the transmission source. The mean percent error is 4%–5%.

TABLE 3
Extrapolated Estimates of μ_t for Thallium-201 Photons

Region	Measured* μ_t for ^{201}Tl	^{241}Am estimates† μ_t for ^{201}Tl	%Error	^{99m}Tc Estimates μ_t for ^{201}Tl	%Error
Heart	0.189	0.186	−1.6	0.191	+1.1
Liver	0.183	0.189	+3.3	0.182	−0.5
Lung	0.0492	0.0497	+1.0	0.0493	+0.2
Spine	0.264	0.314	+18.9	0.250	−5.3
Human‡ bone	0.386	0.431	+11.7	0.327	−15.3%

*Thallium-201 values are regional TCT values averaged from five transaxial slices. These values were validated with narrow-beam geometry transmission measurements using a point source and an HPGe detector. The mean percent error is 4%–5%.
†Americium-241 and ^{99m}Tc estimates of μ_t for ^{201}Tl were determined using collimated values from Table 2 and Equation 11.
‡Human bone values were determined from Reference 13 for E_γ = 75 keV for a bone density of 1.8 g/cm^3.

mined from the lucite plate measurements shown in Figure 5. For ^{241}Am, the contamination is limited to the 75-keV window and $c_e(t)$ is an exponential function whose decay constant is the linear attenuation coefficient of tissue at 60 keV (approximately 0.197/cm), which is expected since the contamination of ^{201}Tl from ^{241}Am results from the overlap of the high energy tail of the ^{241}Am photopeak. Since there is little in-window scattering detected, the function $c_e(t)$ does not significantly deviate from a true exponential function, and subsequently, $f_e(\theta)$ does not vary with tissue thickness and is independent of patient size and projection angle. For ^{99m}Tc, there are separate $c_e(t)$ exponential functions for the 75-keV and 165-keV windows. Since the contamination in the 165-keV window results from the overlap of ^{99m}Tc 140-keV photons, the function $c_e(t)$ for this window decays with linear attenuation coefficient of tissue at 140 keV (approximately 0.153/cm). Because the contamination in the 75-keV window results from lead x-ray production and ^{99m}Tc downscatter, $c_e(t)$ decays at a lower rate of 0.142/cm. Due to this component, $f_e(\theta)$ for ^{99m}Tc exhibits a dependence on patient size and projection angle; greater thicknesses of tissue will produce higher $f_e(\theta)$ values.

For heads 2 and 3, the contamination $b_e(\theta)$ results from transmission photons scattering 120° from the imaged object. Because ^{241}Am photons lose 9 keV by scattering 120°, the overlap of the ^{241}Am photons in the ^{201}Tl window is eliminated, and $b_e(\theta) = 0$ for all θ. For ^{99m}Tc, the $b_e(\theta)$ values for the three patients are displayed in Figure 6. This contamination remained nearly constant for all patients at approximately 90 cps, which is 2.5 times greater than the natural background radiation present in the ^{201}Tl window.

Using the torso phantom transmission data, the effect of axial source collimation on the contamination in the emission window from the transmission source was investigated. There was no change in $f_e(\theta)$ for head 1, but in heads 2 and 3, there was a 10-fold increase in the contamination

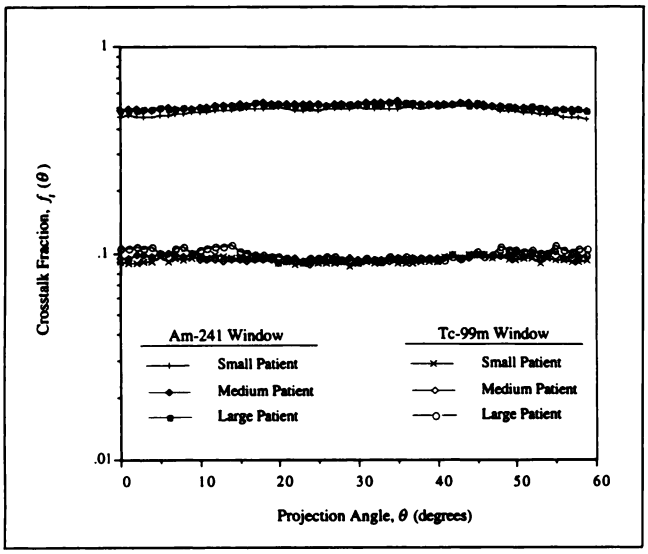

FIGURE 3. Emission-to-transmission crosstalk fraction $f_t(\theta)$ as a function of projection angle and patient size for ^{241}Am and ^{99m}Tc transmission windows.

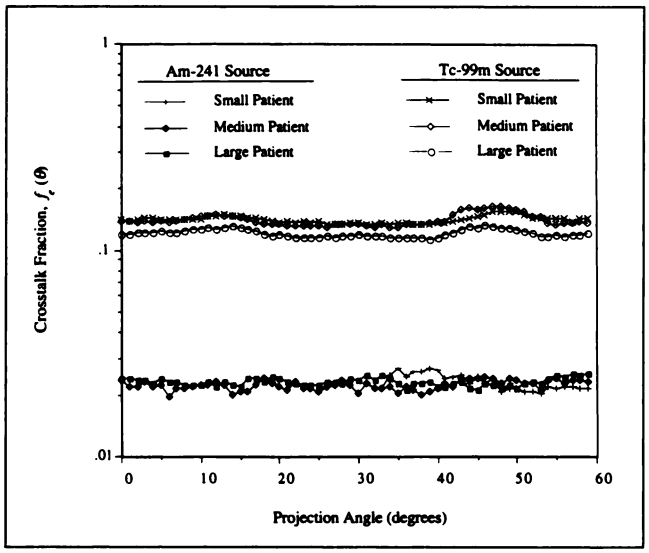

FIGURE 4. Transmission-to-emission crosstalk fraction $f_e(\theta)$ as a function of projection angle and patient size for a detector head collecting transmission and emission data (head 1).

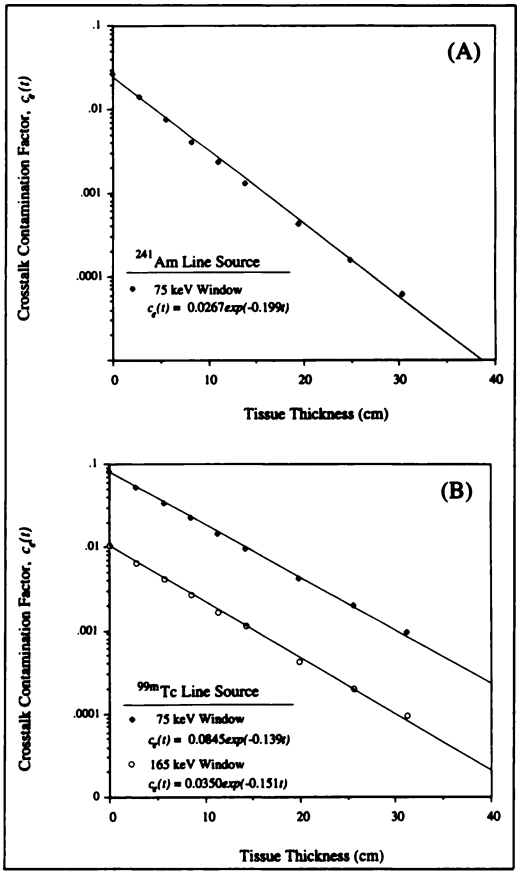

FIGURE 5. Crosstalk correction factor, $c_e(t)$, as a function of tissue thickness for ^{241}Am (A) and ^{99m}Tc (B) line sources. Exponential fits (line curves) are provided for each energy window and transmission source. These $c_e(t)$ curves are valid provided the source is shielded to minimize pulse pile-up and deadtime effects.

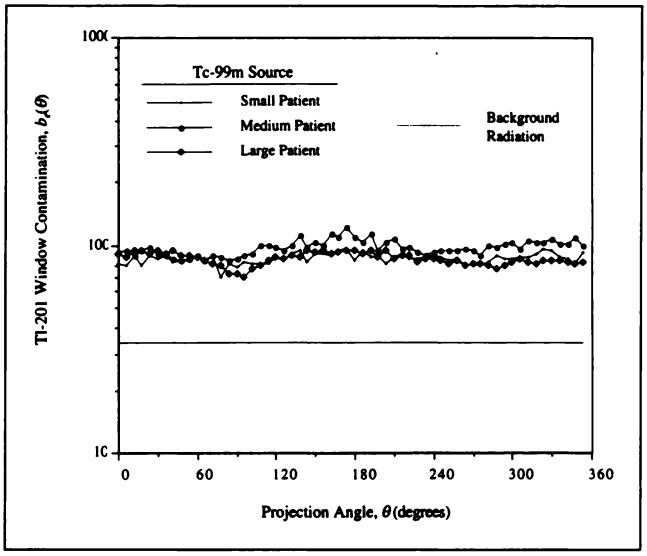

FIGURE 6. Technetium-99m-to-^{201}Tl crosstalk contamination $b_e(\theta)$ as a function of projection angle and patient size for a detector head collecting only emission data (heads 2 and 3) oriented 120° relative to the transmission head.

$b_e(x, y, \theta)$ count rate and a significant change in its spatial distribution between a collimated and uncollimated ^{99m}Tc source. The profile $b_e(x)$ from head 2 in the left lateral view ($\theta = 90°$) is displayed in Figure 7. The peak in $b_e(x)$ for the uncollimated source occurred on the side of the image that was adjacent to the transmission source. Source collimation had no effect on $b_e(x, y, \theta)$ in heads 2 and 3 for an ^{241}Am source.

Table 4 lists the signal-crosstalk emission, $S_e(\theta)$, and transmission, $S_t(\theta)$, values for the large patient and the elliptical chest phantom. Values are reported for posterior (POST) and right anterior oblique (RAO). Differences in $S(\theta)$ values between ^{241}Am and ^{99m}Tc are consistent with the behavior of $f_e(\theta)$, $f_e(\theta)$, and $b_{e2}(\theta)$ previously described. It should be noted that in the absence of source collimation, $S_{e2}(\theta)$ from ^{99m}Tc photons would decrease to 2:1 for the large patient which stresses the importance of axial source collimation. The differences between the patient and phantom $S(\theta)$ values result from the large difference in torso size and the emission rate of the phantom being twice the patient emission rate.

Reconstructed images from the elliptical chest phantom are displayed in Figures 8–10. The difference images represent the absolute difference on a pixel basis between the contaminated or corrected images and the uncontaminated images. The attenuation maps displayed in Figure 8 have been scaled to 75-keV photons using Equation 11. Because the spine insert is teflon, which is a low-Z material, Equation 11 is accurate, and there are no statistically significant differences between the scaled ^{241}Am and ^{99m}Tc maps. In Figure 8, the difference images have been amplified by a factor of 6 for visual display. The mean difference computed on a pixel basis over the attenuation map was −0.00866/cm and 0.00056/cm for contaminated and cor-

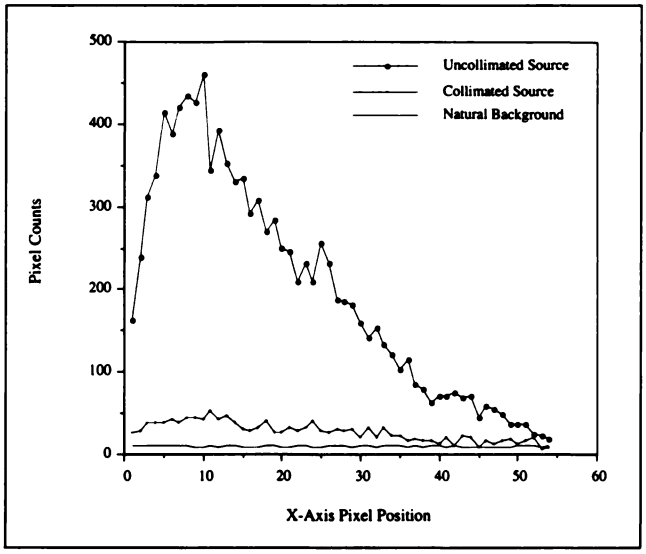

FIGURE 7. Technetium-99m-to-^{201}Tl contamination data $b_{e2}(x, \theta = 90°)$ for a collimated and uncollimated ^{99m}Tc line source. Detector head 2 was in the left lateral position, and the pixel counts were integrated along the y-axis.

TABLE 4
Signal-to-Crosstalk Ratios for Transmission and Emission Data*

	^{241}Am	^{99m}Tc
Large Patient		
S_t	22:1 (POST), 6.7:1 (RAO)	91:1 (POST), 48:1 (RAO)
S_{e1}	4:1 (POST), 12:1 (RAO)	0.8:1 (POST), 1.7:1 (RAO)
S_{e2}	∞	20:1 (POST, RAO)
Chest Phantom		
S_t	10:1 (POST), 3.3:1 (RAO)	43:1 (POST), 19:1 (RAO)
S_{e1}	15:1 (POST), 18:1 (RAO)	2.9:1 (POST), 4.3:1 (RAO)
S_{e2}	∞	100:1 (POST, RAO)

*Subscripts t = transmission data and e = emission data. Numeric subscripts denote camera head number. Data presented for head 2 also apply to head 3 for a triple-head camera.

rected ^{241}Am data and −0.00145/cm and −0.00006/cm for contaminated and corrected ^{99m}Tc data. In terms of mean percent error, there was 1.24% and 0.25% error/pixel in the corrected maps of ^{241}Am and ^{99m}Tc, respectively. These mean percent error values are well within the statistical precision of the transmission measurement.

The emission images from head 1 and head 2 are displayed in Figures 9 and 10, respectively. The contaminated emission images were reconstructed from contaminated transmission *and* emission data and represent the case where no crosstalk corrections are performed. For visual display, the difference images were amplified fourfold in Figure 9, and sixfold in Figure 10. From a three-dimensional region surrounding the heart chamber wall, the mean pixel intensity in the chamber wall was calculated, and the values are presented in Table 5.

DISCUSSION

Based on physical characteristics, ^{241}Am is ideal for routine clinical use due to its 432-yr half-life which eliminates periodic replacement (daily for ^{99m}Tc, yearly for ^{153}Gd and ^{57}Co) and corrections for radioactive decay. The low photon energy of ^{241}Am also provides greater bone-tissue contrast than higher energy photons but requires greater activities of ^{241}Am to achieve transmission rates comparable to ^{99m}Tc. Currently, line source strengths up to 300 MBq/cm (8 mCi/cm) range are commercially available for under $6000 (24 cm in length). Despite the higher source activities of ^{241}Am needed compared to ^{99m}Tc, the whole-body, absorbed dose from 2 to 20-min scans is 0.16 mGy for a 5.55-GBq ^{241}Am source and 0.12-mGy for a 444-MBq ^{99m}Tc source (values measured with a survey meter). These dose rates represent a small fraction of the absorbed dose of 6.6 mGy from 111 MBq of ^{201}Tl radiotracer (based on 0.06 mGy/MBq).

Since the energy of ^{241}Am photons is below the K-edge of lead (88.0 keV), the structure of the source holder can be fashioned from aluminum with lead being used for the shielding and collimation. These materials simplify machining and minimize the size, weight, and cost of the holder. The overall dimensions of our holder are 5.08 × 7.32 × 38.1 and weighs less than 5 kg. The holder provides 9.5 mm of lead shielding around the source which reduces the exposure dose to background levels (<0.2 μGy/hr). As a result of the size, weight and shielding capabilities of the holder, the holder also serves as a home for the ^{241}Am source when it is not in use, which eliminates handling and the possibility of a radiation accident with a long-lived alpha emitter.

For transmission sources such as ^{99m}Tc with photon energies greater than 88 keV, x-rays are produced in the lead shielding and collimation of the holder which contaminates the ^{201}Tl data. Measurements with our holder showed that 40%–45% of the ^{99m}Tc contamination in the

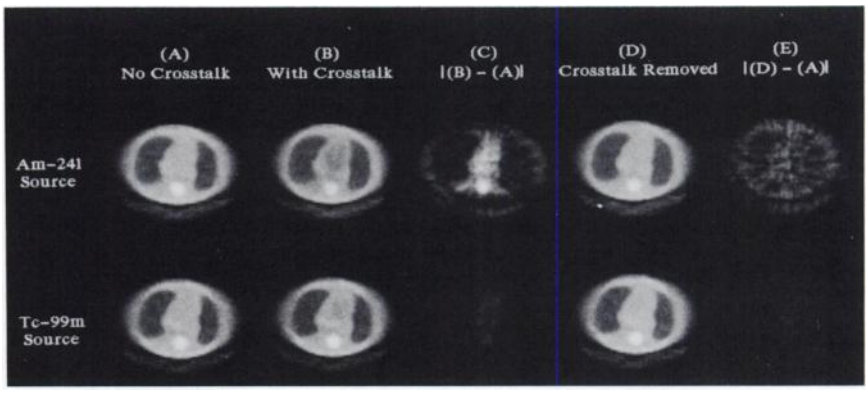

FIGURE 8. Reconstructed attenuation maps of elliptical chest phantom for 75 keV photons. Maps were reconstructed from uncontaminated (A), contaminated (B) and corrected (D) transmission data for ^{241}Am and ^{99m}Tc transmission sources. Absolute difference images were computed for the contaminated (C) and corrected (E) maps as compared to the uncontaminated map. The amplitude of the difference images has been increased sixfold for visual display.

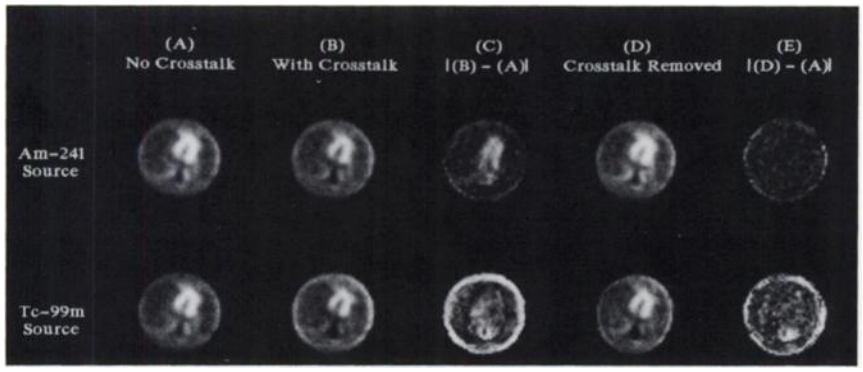

FIGURE 9. Attenuation-corrected transaxial emission images of the elliptical chest phantom using emission projections from head 1 and the attenuation maps of Figure 8. Images were reconstructed using uncontaminated (A), contaminated (B) and corrected (D) emission *and* transmission data for ^{241}Am and ^{99m}Tc transmission sources. Absolute difference images were computed for the contaminated (C) and corrected (E) images as compared to the uncontaminated images. The amplitude of the difference images has been increased sixfold for visual display.

^{201}Tl window resulted from lead photons produced by the source holder. Therefore, to improve the emission signal-to-crosstalk ratio for ^{99m}Tc, copper or tin should be used for slit collimation, and either tungsten or lead surrounded by copper for the shielding. However, the exclusion of lead makes the construction of the holder more difficult to machine and more expensive. The holder will also be slightly larger and heavier due to the higher energy photons that must be shielded.

Both ^{241}Am and ^{99m}Tc transmission sources can accurately measure attenuation distribution in the thorax. However, based on the results for bone in Table 3, linear extrapolation is a poor approximation for converting measured μ_t for bone from the transmission energy to the emission energy. Simulations are necessary to determine the effect that these inaccurate bone estimates will have on the attenuation-corrected emission data. If the error propagation due to the errors in bone attenuation is significant, then the bone must be segmented from the surrounding tissue and scaled separately. Segmentation can be more easily accomplished on the high contrast images of ^{241}Am. The increased contrast of ^{241}Am also aids in the correlation of anatomical and physiological data from the superimposition of TCT and SPECT data.

A significant decrease in μ_t values was not seen in the absence of source collimation because the line source is positioned at the focal length of the converging collimator which minimizes the probability of once-scattered photons being counted. Although source collimation had little effect on the measured μ_t values, it significantly decreased $b_e(x, y, \theta)$ in heads 2 and 3 (cf., Fig. 7). Axial source collimation on the ^{99m}Tc source decreased $b_{e2}(\theta)$ from 610 cps to 90 cps (background is 35 cps), and removed almost all of the spatial variation in the contamination data. Source collimation also decreased the count rate of scattered ^{241}Am photons detected in the ^{241}Am window in heads 2 and 3 from 500 cps to 30 cps which is essential to the assumption that $P_t(x, y, \theta) = 0$ so that $b_{t1}(x, y, \theta) = b_{t2}(x, y, \theta)$.

The transmission signal-to-crosstalk ratio is approximately five times greater for ^{99m}Tc compared to ^{241}Am. The effect of this contamination is clearly seen in the elliptical phantom difference images (column C) of Figure 8. As expected, most of the contamination is in the heart and surrounding tissue which reduces the μ_t values in this region. Upon correcting the projections for crosstalk using the contamination measured by head 2, the resulting corrected attenuation map is not statistically different from the uncontaminated map (column E).

The data presented in Table 5 reflects the error in the reconstructed attenuation images due to the presence and removal of crosstalk from the emission and transmission data. For head 1, contaminated emission data reconstructed with contaminated transmission data reduced the mean counts in the heart wall by 13% and 9.8% for ^{241}Am and ^{99m}Tc, respectively. For ^{241}Am, the reduction is due to the artifact in the attenuation map, while for ^{99m}Tc, the reduction is due primarily to the crosstalk in the emission data. Upon removal of the crosstalk from the emission and transmission data, the percent change in the mean was 1.4% and −8.5% for ^{241}Am and ^{99m}Tc, respectively. To

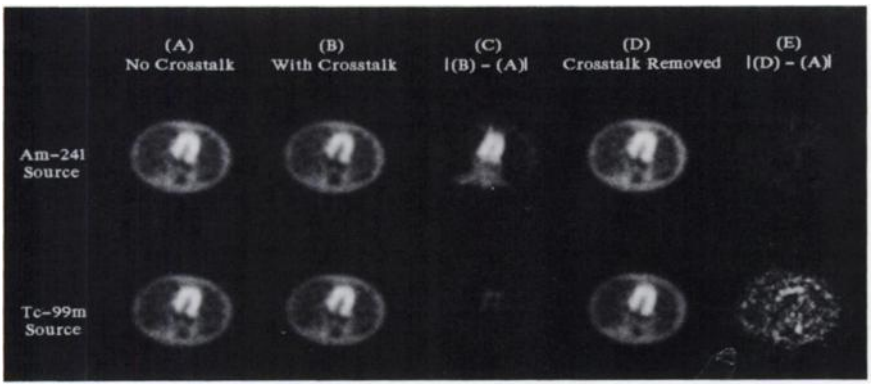

FIGURE 10. Attenuation-corrected transaxial emission images of the elliptical chest phantom using summed emission projections from heads 2 and 3 and the attenuation maps of Figure 8. Images were reconstructed using uncontaminated (A), contaminated (B) and corrected (D) emission *and* transmission data for ^{241}Am and ^{99m}Tc transmission sources. Absolute difference images were computed for the contaminated (C) and corrected (E) images as compared to the uncontaminated images. The amplitude of the difference images has been increased fourfold for visual display.

TABLE 5
Mean Pixel Counts in Reconstructed Heart Chamber Wall of the Elliptical Chest Phantom

	^{241}Am	^{99m}Tc
Emission Head 1		
Uncontaminated emission and transmission data	1253 ± 13	1242 ± 13
Contaminated emission and transmission data	1085 ± 12	1120 ± 14
Contaminated emission with corrected transmission data	1249 ± 14	1167 ± 14
Corrected emission and transmission data	1271 ± 14	1136 ± 14
Emission Heads 2 and 3		
Uncontaminated emission and transmission data	1266 ± 11	1243 ± 11
Contaminated emission and transmission data	1079 ± 9	1203 ± 10
Contaminated emission with corrected transmission data	1268 ± 11	1237 ± 12
Corrected emission and transmission data	1268 ± 11	1161 ± 9

estimate the error resulting solely from the removal of emission crosstalk, the contaminated emission data were reconstructed with corrected transmission data. For this case, the percent change in the mean counts in the heart changed by −0.3% and 6.0% for ^{241}Am and ^{99m}Tc sources, respectively. Based on these data, there is not a significant improvement when the crosstalk in the emission data is removed. This was not unexpected since only a small fraction of the crosstalk is directly in the heart (most is in the lungs as seen in column C of Figure 9), but the data also suggest that crosstalk compensation techniques need further improvement.

For head 2, contaminated emission data reconstructed with contaminated transmission data reduced the mean counts in the heart wall by 15% and 3.2% for ^{241}Am and ^{99m}Tc, respectively. Upon removal of the crosstalk from the emission and transmission data, the percent change in the mean was 0.2% and −6.6% for ^{241}Am and ^{99m}Tc, respectively. For the case using contaminated emission data with corrected transmission data, the percent change in the mean counts in the heart changed by 0.2% and −0.5% for ^{241}Am and ^{99m}Tc sources, respectively. For ^{99m}Tc data, there is less error in images using contaminated emission data compared to corrected emission data when reconstructing with corrected transmission data. This behavior results from Equation 7 which approximates the crosstalk in the emission data by assuming that the projection counts in the region of the heart are statistically identical between heads 2 and 3. The slight differences in the heads of our system coupled with noisy data biases the crosstalk estimate and subsequently introduces additional error into the reconstructed images. Based on these results and because the emission signal-to-crosstalk ratio for ^{99m}Tc is large and the crosstalk is fairly uniform (provided source collimation is used), it is suggested that the crosstalk from ^{99m}Tc in the emission data of heads 2 and 3 be ignored.

Provided the crosstalk into the transmission data is measured (i.e., multihead system, single-head system with a scanning line source), ^{241}Am introduces less error into the attenuation-corrected ^{201}Tl emission images than ^{99m}Tc, and should be strongly considered for transmission imaging during ^{201}Tl SPECT. It should also be noted that the benefits of ^{241}Am transmission images during ^{201}Tl SPECT are also apparent in ^{99m}Tc SPECT, since the photon energy of ^{241}Am is less than 140 keV. For ^{99m}Tc SPECT, there is the additional benefit of no overlap between the photopeaks of ^{241}Am and ^{99m}Tc. As a result, there is no crosstalk in the emission data of head 1, and the crosstalk in the ^{241}Am transmission data from ^{99m}Tc will be less severe than the crosstalk from ^{201}Tl. Therefore, TCT with ^{241}Am can be performed during both ^{201}Tl and ^{99m}Tc cardiac SPECT with the same crosstalk compensation techniques being employed. None of the other isotopes in Table 1 offer this benefit.

CONCLUSION

Measured attenuation maps of the thorax are necessary to correct cardiac SPECT studies for photon attenuation. Systems employing simultaneous transmission-emission tomography do not increase the patient imaging time and do not suffer from image registration problems. Compared to a ^{99m}Tc transmission source, ^{241}Am yields higher signal-to-crosstalk ratios for the emission data and is more convenient for routine clinical use.

ACKNOWLEDGMENTS

The authors thank the Physics Machine Shop at the University of Michigan for their help in the design and fabrication of the line source holder. The comments and suggestions of Robert Ackermann regarding the implementation of a TCT-SPECT system are also appreciated. This work was supported by NCI grant CA09015, NIH grant RO1 HL41047 (M.S.), the NIH grant RO1 CA32846 (W.L.R.), NCI grant CA60711 (J.A.F.), and the DOE Alexander Hollander Fellowship Award (J.A.F.). This work was completed during the tenure of an Established Investigatorship from the American Heart Association (M.S.).

REFERENCES

1. Malko JA, Gullberg GT, Kowalsky WP, Van Heertum RL. A count-based algorithm for attenuation-corrected volume determination using data from an external flood source. *J Nucl Med* 1985;26:194–200.
2. Malko JA, Van Heertum RL, Gullberg GT, Kowalsky WP. SPECT liver imaging using an iterative attenuation correction algorithm and an external flood source. *J Nucl Med* 1986;27:701–705.
3. Tsui BM, Gullberg GT, Edgerton ER, et al. Correction of nonuniform attenuation in cardiac SPECT imaging. *J Nucl Med* 1989;30:497–507.
4. Bailey DL, Hutton BF, Walker PJ. Improved SPECT using simultaneous emission and transmission tomography. *J Nucl Med* 1987;28:844–851.
5. Manglos SH, Bassano DA, Thomas FD. Cone-beam transmission computed tomography for nonuniform attenuation compensation of SPECT images. *J Nucl Med* 1991;32:1813–1820.

6. Manglos SH, Bassano DA, Thomas FD, Grossman ZD. Imaging of the human torso using cone-beam transmission CT implemented on a rotating gamma camera. *J Nucl Med* 1992;33:150–156.
7. Frey EC, Tsui BM, Perry JR. Simultaneous acquisition of emission and transmission data for improved ^{201}Tl cardiac SPECT imaging using a ^{99m}Tc transmission source. *J Nucl Med* 1992;33:2238–2245.
8. Tung C-H, Gullberg GL, Zeng GL, Christian PE, Datz FL, Morgan HT. Nonuniform attenuation correction using simultaneous transmission and emission converging tomography. *IEEE Trans Nucl Sci* 1992;39:1134–1143.
9. Tan P, Bailey DL, Meikle SR, Eberl S, Fulton RR, Hutton BF. A scanning line source for simultaneous emission and transmission measurements in SPECT. *J Nucl Med* 1993;34:1752–1760.
10. Jaszczak RJ, Gilland DR, Hanson S, Jang KL, Greer KL, Coleman RE. Fast transmission CT for determining attenuation maps using a collimated line source, rotatable air-copper-lead attenuators and fan-beam collimation. *J Nucl Med* 1993;34:1577–1586.
11. Weber DA, Eckerman KF, Dillman LT, Ryman, JC. *MIRD: radionuclide data and decay schemes*. New York: The Society of Nuclear Medicine; 1989.
12. Lederer CM, Shirley VS, eds. *Table of isotopes, 7th edition*. New York: Wiley; 1978.
13. Hubbell, JH. Photon cross sections, attenuation coefficients, and energy absorption coefficients from 10 keV to 100 GeV. *NSRDS-NBS* 29, 1969.
14. Sauer K, Bouman C. A local update strategy for iterative reconstruction from projections. *IEEE Trans Signal Proc* 1993 Feb;41:523–548.
15. Fessler JA. Penalized, weighted least squares image reconstruction for positron emission tomography. *IEEE Trans Med Imaging* 1994: in press.
16. Lewitt RM. Processing of incomplete measurement data in computed tomography. *Med Phys* 1979;6:412–417.
17. Nalcioglu O, Cho ZH, Lou RY. Limited field of view reconstruction in computerized tomography. *IEEE Trans Nucl Sci* 1979;NS-26: 546–551.

Condensed from
30 Years Ago:

Measurement of Pericardial Fluid Correlated with the Iodine-131-Cholografin® and IHSA Heart Scan

David M. Sklaroff, N. David Charkes, and Dryden Morse
Departments of Radiology and Thoracic Surgery, Albert Einstein Medical Center, Northern Philadelphia, Pennsylvania

Since its introduction, the radioisotope heart scan has become established as a safe, simple, and useful technique for the diagnosis of pericardial effusion. Nevertheless, few studies have been reported concerning quantitative aspects of the method. It was proposed that a preoperative heart scan be performed and the pericardial contents aspirated and measured in all such patients, and that criteria for heart scanning be established from these figures.

To date, 23 operated patients have been so studied. In addition, data was available from postmortem examination in six other patients, and five patients with pericardial effusion underwent diagnostic pericardiocentesis. An additional three patients had massive pericardial effusions but were not tapped; these patients are also included in the series.

Iodinated human serum albumin-I^{131} (IHSA) in doses of 4-6 μCi/kg was employed as the scanning agent, as in the original investigations. Since April, 1961, we have employed I^{131}-Cholografin® and at present it is used exclusively.

Iodius-131-Cholografin is extracted from the blood by the polygonal cells of the liver and is then excreted into the biliary tree. The rate of extraction is such that 50% of the initial blood concentration disappears within 4.8 hr (if 0.25 mg Cholografin is injected). The scan is begun 15 min after injection at the sternal notch and proceeds caudally, so that by the time the liver is reached (40-60 min) about 10%-15% of the Cholografin has been removed from the blood. Satisfactory scans have been obtained with doses of I^{131}-Cholografin of 3-7 μCi/kg and scan speeds of 16-18 cm/min. Nonradioactive iodine is administered orally several hours prior to scanning to block the thyroid uptake.

The instrument used for this study was the Picker Magnascanner, which is equipped with a 3 × 2-inch NaI(TA) crystal and pulse-height analyzer. The maximum count rate varied somewhat with the dose, blood volume, cardiac size and geometry, but was approximately between 6 and 15 cpm/μCi (1800-6000 cpm).

The scan was displayed both on Teledeltos paper and on clear x-ray film, but only the latter was used for diagnostic purposes (photoscan). Localizing marks were made in the midclavicular lines at approximately the fourth intercostal space and recorded on the photoscan. Lead shots were then placed on the skin marks and two successive exposures made of the chest at a 6-foot distance in the AP projection, the central ray passing through the lead markers alternately.

The photoscan was then accurately superimposed on the roentgenogram and the maximum transverse cardiac diameters measured. Comparison of these parameters proved to be the best criterion of pericardial effusion.

Of the 37 patients, 13 had pericardial effusions of 200 cc or more. The other 24 patients all had severe cardiac disability, with hypertrophy and/or dilatation of one or more chambers. These latter patients, with effusions of 100 cc or less, were compared with the group of 13.

In the 24 patients with cardiac hypertrophy and/or dilatation with 100 cc or less of pericardial fluid, the mean difference between the maximum transverse cardiac diameters on scan and x-ray was 2.1 cm and was always less than 3.5 cm. The ratio of the two diameters was always greater than 0.80.

There were 13 patients with pericardial effusions of 200 cc or greater and in 11 of these, the difference between the maximum transverse cardiac diameters of scan and x-ray was greater than 4.5 cm. The ratio of the diameters in every case was less than 0.80 (mean 0.69).

With marked pericardial effusion (Fig. 1b) a nonradioactive zone visibly surrounds the cardiac blood pool, and separation from the pulmonary vasculature and from the liver can be demonstrated. These changes are more obvious when the scan is seen without superimposition on x-ray.

(continued on page 671)